BIOCHEMISTRY
including biophysical chemistry & molecular biology
Article

Biochemistry **2010,** *49,* 10061–10071 10061
DOI: 10.1021/bi101229m

A pH-Dependent Conformational Ensemble Mediates Proton Transport through the Influenza A/M2 Protein†

Alexei L. Polishchuk,‡ James D. Lear,*,‡ Chunlong Ma,§ Robert A. Lamb,∥ Lawrence H. Pinto,§ and William F. DeGrado*,‡

‡*Department of Biochemistry and Biophysics, School of Medicine, University of Pennsylvania, Philadelphia, Pennsylvania 19104-6059, United States,* §*Department of Neurobiology and Physiology, and* ∥*Department of Biochemistry, Molecular Biology and Cell Biology and Howard Hughes Medical Institute, Northwestern University, Evanston, Illinois 60208-3500, United States*

Received August 2, 2010; Revised Manuscript Received October 21, 2010

ABSTRACT: The influenza A/M2 protein exhibits inwardly rectifying, pH-activated proton transport that saturates at low pH. A comparison of high-resolution structures of the transmembrane domain at high and low pH suggests that pH-dependent conformational changes may facilitate proton conduction by alternately changing the accessibility of the N-terminal and C-terminal regions of the channel as a proton transits through the transmembrane domain. Here, we show that M2 functionally reconstituted in liposomes populates at least three different conformational states over a physiologically relevant pH range, with transition midpoints that are consistent with previously reported His37 pK_a values. We then develop and test two similar, quantitative mechanistic models of proton transport, where protonation shifts the equilibrium between structural states having different proton affinities and solvent accessibilities. The models account well for a collection of experimental data sets over a wide range of pH values and voltages and require only a small number of adjustable parameters to accurately describe the data. While the kinetic models do not require any specific conformation for the protein, they nevertheless are consistent with a large body of structural information based on high-resolution nuclear magnetic resonance and crystallographic structures, optical spectroscopy, and molecular dynamics calculations.

The influenza virus infects cells by receptor-mediated endocytosis, which is followed by acid-induced fusion of the viral and endosomal membranes. The fusion event is mediated by a conformational change of the influenza hemagglutinin proteins, triggered by the low pH in the endosome lumen (*1*). It is also necessary, upon fusion, that the viral interior be acidified for the viral RNA to be freed in a competent form into the cell cytoplasm (*2*). Viral acidification within the time of endosomal residence requires a proton transport facilitator denoted "M2" (matrix protein 2), a 97-residue homotetrameric integral membrane protein (*3*). In addition, it has been shown that influenza strains with higher pH values for the transition of hemagglutinin from the prefusion to the fusion-competent state also require proton transport through M2 when newly synthesized viral proteins are trafficked in the Golgi apparatus (*4*). At this point in the infection cycle, M2 transports protons out of the slightly acidic Golgi lumen to protect the hemagglutinins from a premature transition into the fusion-competent state. The proton transport function of M2 is inhibited by the antiviral compounds amantadine and rimantadine (*5*), which have been mainstays of influenza treatment for more than three decades. However, in recent years, many circulating influenza A virus strains have developed resistance to amantadine and its derivatives (*6*), prompting renewed interest in the structure and function of the essential M2 protein in the hope of designing alternative inhibitors (see, e.g., refs *7* and *8*).

The goal of this work is to understand how M2's complex proton-dependent conformational transitions contribute to its proton flux activity. M2 is one of the smallest membrane proteins known to mediate ion transport, yet well-defined segments of its extramembrane sequence have been implicated in other roles in the viral life cycle, indicative of a multifunctional, modular protein (*9*). Although this work focuses exclusively on the full-length protein, a very small peptide corresponding to the M2 transmembrane segment was recently shown to reproduce the ion transport, drug sensitivity, and tetramer assembly properties of full-length M2 (*10*). This finding paved the way for detailed mechanistic correlation of whole-cell electrophysiology studies of the full-length protein with results of structural and biophysical experiments involving the transmembrane segment.

Extensive electrophysiological characterization (*11*−*20*) has established that His37 protonation is part of the conduction process and is responsible for the extreme proton selectivity observed for M2 (*21*, *22*), while Trp41 is required for inward rectification of current (*18*). Protonation of His37 is important for "activation" of the channel, having a pK_a near 6. However, the mechanism of "gating" and conduction through the channel remains to be fully elucidated. There is now general agreement (*10*, *15*, *22*−*24*) that M2 conducts on the order of 1−1000 protons per second under conditions of an outer pH (pH_{out}) between 7 and 5, pH_{in} 7, and an electrical gradient from 0 to 130 mV driving inward proton flux. These rates are far lower than those of potassium or other cation channels that transport ions, under

†This research was supported by National Institutes of Health Grants R01AI57363 to L.H.P. and U011074741 to W.F.D. and R.A.L. R.A.L., L.H.P., and W.F.D. are founders and members of the SAB of Influmedix (http://www.influmedix.com).

*To whom correspondence should be addressed. W.F.D.: telephone, (215) 898-4590; fax, (215) 537-7229; e-mail, wdegrado@mail.med.upenn.edu. J.D.L.: telephone, (215) 898-2071; e-mail, jamesdlear@comcast.net.

Published on Web 10/22/2010

conditions in which their conducted ions are at physiological concentrations, typically 0.15 M. As discussed by Decoursey (*25*) and Zhou (*26*), the difference in the absolute rate between M2 and traditional typical potassium channels does not imply that protons necessarily need to overcome a large energy barrier while traveling through the M2 channel. In fact, within the physiological pH range of pH_{out} 5−7, the overall second-order rate constants for proton entry and conduction through M2 are equal to 10^7−10^9 M^{-1} s^{-1}, which are close to the diffusion-controlled limit for a proton diffusing through a pore with the dimensions of the M2 channel. Thus, the slow rate of conduction does not necessarily reflect the presence of large energy barriers within the channel but rather is a simple consequence of the very low proton concentration over the physiological pH range. Therefore, the channel operates within a couple orders of magnitude of the maximal rate possible over the endosomal pH range.

A particularly interesting feature of M2 is the fact that the rate of proton flux through the channel does not scale linearly with the proton concentration when the pH is lowered below the physiologic but instead levels as the pH is decreased below 5 (*11*, *27*). This behavior contrasts with that of simple cation-selective channels such as gramicidin or model peptides that lack ionizable side chains; with a modest electrical potential, these channels have an extrapolated conductance of 100 protons/s at pH 6 (10^{-6} M hydronium) and 10^8 protons/s at pH 1.0 (0.1 M hydronium ion) (*25*). A variety of mechanisms can be devised to account for saturation, based on classical channel-like or site binding models. In a classical channel gating model (*28*), the pH-dependent activation of M2 conduction would be associated with protonation of the third His37 residue of the tetrad [$pK_a \sim 6$ (*29*)], explaining the activation of the channel as the pH is lowered between pH 7 and 5. The saturation of the rate at still lower pH_{out} values can occur when the entry of protons into the channel, which is dependent on proton concentration, is much more rapid than the subsequent transit through the channel, which in the simplest case is independent of the bulk proton concentration. This scenario, which is functionally equivalent to a saturable binding isotherm, leads to accumulation of one or more protons in the pore impeding further flux and accounting for the leveling of the flux at low pH_{out}.

A related model seeks to explain the conductance of the channel in terms of the protonation and/or deprotonation of His37, which serves to shuttle protons through the channel (*14*, *15*). This model has been expanded to include structural and dynamic details as crystallographic, NMR,[1] and spectroscopic studies have become available (*26*). ssNMR studies of the M2 TM domain in bilayers (*29*) have shown that the pK_a values for successive protonations of His37 in the tetramer (designated +0 through +4) are 8.2, 8.2, 6.3, and ≤5; equilibrium studies of full-length M2 in micelles were consistent with these values (*10*). Moreover, a number of NMR studies of M2 in micelles and bilayers have shown that the backbone conformation of M2 is reasonably well-defined in states +0 through +2 but becomes more dynamic upon addition of the third proton, with a pK_a of 6.3 (*30*, *31*). Conformational dynamics involving both the main chain amides and the Trp41 side chain occur on the microsecond to millisecond time scale in the +3 state (*31*). Several important points from these studies need to be emphasized. The fact that the +3 state is seen to be in dynamic equilibrium indicates that there is a relatively small energy difference between the different conformational states (at most a few kilocalories per mole), and this energetic difference is well within the energetic variation expected for different environments (e.g., crystals and micelles). Thus, high-resolution structures should be viewed as members of a low-energy ensemble, rather than specifically identified with a given protonation state. Second, the observed dynamics indicate that the protein undergoes large-scale conformational fluctuations on the same time scale as the rate of proton transport. Finally, various high-resolution structures (*31*−*33*) and molecular dynamics calculations (*34*, *35*) have shown that the protein has distinct conformational states that differ with respect to the size of the opening of the pore at either end of the bundle, which dilate and contract in a reciprocal manner.

Structure-based models suggest that M2 exists in an equilibrium between conformers that are more open at the N-terminal entryway and C-terminal exit of the channel, encouraging diffusion into and out of the channel (*26*, *34*). An analysis of available high-resolution structures (*33*) and molecular dynamics studies (*34*) suggests the presence of several conformational variants at equilibrium, described in this work as states "A", "B", and "C" (Figure 1). Here, state A resembles the high-pH solution NMR structure (*31*), and states B and C represent models from intermediate-pH (*32*, *33*) and low-pH crystal structures (*32*), respectively. Molecular dynamics simulations suggest that the populations of M2 conformations are sensitive to the state of protonation of His37 (*34*), and NMR studies show that they are able to change on the same time scale as proton transit through the channel (*31*). In the His relay model (*14*), the third proton is expected to bind to the His37 tetrad with each turnover of the channel. The saturation of rate occurs at low pH when the site is fully occupied and is limited by the off rate for deprotonation. More recent crystallographic studies suggest that this site might instead be considered a cluster of His side chains and water molecules (*33*). In either case, the rate of deprotonation of a site with a pK_a is given by the ratio of rate constants for deprotonation and protonation, placing an upper limit of 10^3 s^{-1} for a pK_a of 6 and a second-order rate constant of 10^9 M^{-1} s^{-1} for diffusion of a proton into a water-filled pore (*25*). The actual rate will depend on the fractional population of different conformational states and the proton permeabilities of the N-terminal and C-terminal sections of their pores.

Previous attempts to model the highly asymmetric conductance of M2 using a simple single-site model without the possibility of conformational changes resulted in a good fit for most experimental conditions but either did not consider (*26*) or failed to explain the low conductance when protons flow in the reverse direction with low pH_{in} and high pH_{out} (*36*). We therefore wished to examine whether the structural changes, such as those observed in recent NMR and crystallographic structures obtained in detergent micelles (*31*−*33*), might better explain the extensive conductance−voltage curves available for the protein (*11*, *12*). It was first important to ascertain that the pK_a values previously determined via ssNMR for the TM domain were consistent with the behavior of the full-length protein in a nativelike, bilayer environment where proton conduction through M2 could be demonstrated. We therefore conducted measurements of the solvent accessibility of the critical Trp41 residue of full-length A/M2 as a function of pH when the protein was functionally reconstituted in liposomes. The results were fully in accord with

[1]Abbreviations: POPC, 1-palmitoyl-2-oleoyl-*sn*-glycero-3-phosphocholine; POPG, 1-palmitoyl-2-oleoyl-*sn*-glycero-3-phospho-(1′-*rac*-glycerol); OG, octyl β-D-glucopyranoside; NMR, nuclear magnetic resonance; TM, transmembrane; ss, solid state.

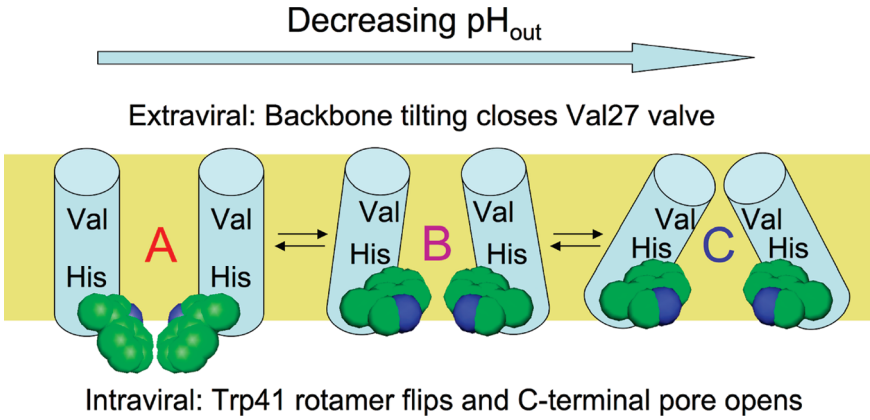

FIGURE 1: Proposed trajectory of structural transitions in the M2 transmembrane domain as a function of extraviral pH. The A conformation is based on an NMR structure in micelles at high pH (*31*); the intermediate B conformation is proposed from molecular dynamics experiments on M2 protonation states (*34*) and intermediate-pH crystal forms of the tetramer (*33*), while the C conformation is based on a crystal structure of M2 at low pH (*32*). The helix bundle is depicted side-on with the front two helices removed. The proposed conformational changes upon a reduction in N-terminal pH involve closure of the N-terminal Val27 valve with an increase in the helix tilt at the top of the bundle, while at the C-terminal end of the bundle, the Trp41 side chains (space filling representation) undergo a rotamer shift and then separate as a result of increased helix tilt. These changes control exposure of the proton-binding His37 side chains near the middle of the bundle to N-terminal and C-terminal pore waters.

the earlier study of the TM peptide that measured His37 pK_a values (*29*) and suggest that the solvent accessibility of Trp41 in the context of functional, full-length A/M2 changes with the His37 tetrad protonation state. These pK_a values, now validated for the full-length, functionally reconstituted protein, provided important experimental input to help constrain fitting of additional parameters necessary to fully define the conductance model. Additionally, the parallel changes of Trp41 solvent accessibility and His37 tetrad protonation suggest that the TM domain of M2 may undergo distinct conformational transitions in bilayers as a function of His37 tetrad protonation state, consistent with the differing conformations seen in high-resolution micelle structures of the TM domain (*31*−*33*) obtained at different pH values.

Having constrained the model with experimental parameters, we examined scenarios in which proton dissociation versus conformational changes were modeled to be rate-determining and found the best agreement with experimentally determined flux values when deprotonation became at least partially rate-determining at low pH. While the results of the fitting do not require any specific structural model, they are consistent with a body of structural data and MD calculations of the M2 proton channel.

MATERIALS AND METHODS

Monitoring Conformational Changes of M2 Trp41 in Bilayers. Stern−Volmer fluorescence titrations (*37*) of M2 Trp41 at varying pH values were used to track pH-dependent conformational changes of M2. The WT A/Udorn/72 sequence (accession number CAD22815) has two Trp residues (at positions 15 and 41), which would have complicated spectral analysis. A synthetic gene encoding a single-Trp, Cys-free full-length Udorn A/M2 construct with a six-His C-terminal tag was therefore obtained with codon usage optimized for expression in *Escherichia coli* (Midland Certified Reagent Co., Midland, TX). BL21 cells were transformed with the pET23D(+) plasmid containing the M2 gene using chemical or heat shock methods. The protein was expressed and purified from *E. coli* as previously described (*10*). The single-Trp variant used retained the Trp side chain at position 41 in the transmembrane domain and had a Trp15Phe mutation to simplify data analysis without compromising transport function (*10*). In addition, this Cys-free construct provided the high culture yields of the protein necessary for these experiments.

To allow detection of Trp41 fluorescence, a target protein monomer:lipid ratio of 1:100 was used. POPC and POPG were purchased as presealed chloroform stocks from Avanti Polar Lipids (Alabaster, AL). Cholesterol powder (Sigma grade, Sigma-Aldrich, St. Louis, MO) was dissolved in chloroform immediately prior to use. Lipid films (25 μmol total of a 4:1:2 POPC/POPG/cholesterol mixture), made by evaporating chloroform stocks under a stream of argon, were thoroughly hydrated with ~400 μL of Milli-Q water and 100 μL of 10× buffer [500 mM $K_xH_xPO_4$ and 100 mM NaCl (pH adjusted to 7.0 with HCl)]. The actual volume of water added was adjusted so that following the subsequent addition of protein, the total volume of the sample would be 1 mL. The sample was vigorously vortexed, and the hydrated, protein-free lipid suspensions were subjected to six freeze−thaw cycles (dry ice/ethanol bath and 37 °C water bath).

Full-length A/M2 [Cys-free, Trp15Phe His-tagged variant as buffer-exchanged eluate from the nickel column, in 50 mM HEPES (pH 8), 4 mM OG, and 20% (v/v) glycerol, which ran as a single band on a native protein gel] was next added dropwise to the experimental sample. The stock concentration of the protein monomer was ~500 μM. For the control liposome sample, an equal volume of protein-free HEPES/OG/glycerol buffer was added. The mixtures were frozen and thawed six additional times and sized to a 100 nm liposome target diameter by at least 33 passes through a mini-extruder (Avestin, Ottawa, ON). To remove residual OG from the samples, the mixtures were dialyzed for one or two cycles in 1 L of 1× buffer [50 mM $K_xH_xPO_4$ (pH 7.0) and 10 mM NaCl] in the presence of the detergent-binding resin Amberlite XAD-4 (Supelco, Bellefonte, PA).

For experiments, 20 μL of a liposome suspension was added to 2 mL of 1× buffer set at the desired pH. Measurements were performed in a 1 cm × 1 cm Hellma (Plainview, NY) QS fluorescence cell. Ten microliters of a 4 μM ethanolic stock of the protonophore FCCP (Fluka/Sigma-Aldrich, St. Louis, MO) was added to dissipate the pH gradient. The mixture was stirred for 5 min following FCCP addition prior to the experiment. A reference cuvette similarly configured but with control liposomes

added at pH ~7 was used for online subtraction of the background signal from scatter induced by the vesicles.

We performed experiments while samples were stirred in an Aviv (Lakewood, NJ) ATF-105 spectrofluorometer at 25 °C by measuring a baseline Trp fluorescence value at the end of the 5 min equilibration period, then adding 50 μL aliquots of a 5 M NaI solution (also containing 1 mM $Na_2S_2O_3$ to prevent I^- photooxidation), and taking measurements following the addition of every aliquot. An automated titrator (Hamilton, Reno, NV) allowed for high-precision titrant addition with automated timing of sample equilibration and data acquisition. No titrant was added to the control cuvette, and the subtracted background signal was not corrected for the small dilution effect on the reference signal (~10% maximum) that addition of titrant would have caused. To account for any deviation from the preset buffer pH as a result of addition of other sample components, the sample pH was measured at the conclusion of each titration, and that value was used as the experimental pH.

To avoid exciting Tyr residues in the protein, fluorescence excitation was performed at 295 nm. Fluorescence emission was measured at 340 nm, near the average emission maximum of indole in both hydrophobic and polar environments.

The measurement of intrinsic Trp fluorescence in bilayers can be complicated by substantial scatter artifacts from the liposome sample (*38*). We minimized scattering by installing polarizers in a cross-polarized configuration (excitation polarizer horizontal, emission polarizer vertical) and adding an emission filter that blocked light at wavelengths below 300 nm from reaching the detector. The excitation bandwidth was kept lower (2−3 nm) than the emission bandwidth (6−7 nm). As a control, quenching experiments using this configuration with model Trp-like small molecule compounds were performed (data not shown) and yielded quenching constant values consistent with those available in the literature (*39*, *40*).

We observed that the steady-state Trp fluorescence of M2 in liposomes was somewhat unstable (and declining) as a function of time, especially at certain pH values. A variety of factors were adjusted in an attempt to account for this phenomenon, including the length and frequency of sample irradiation (to rule out photooxidation), the length of temperature equilibration, and the presence and absence of various ionophores such as FCCP and valinomycin. None of these appeared to be causally involved. The experiment was therefore performed under very stringent and consistent timing by using the autotitrator, and the initial, unquenched fluorescence value in the data analysis was normalized to 1 using a fitted linear error parameter (see below).

Quenching Data Analysis. Fluorophores such as the indole group of tryptophan, when in their excited electronic state (which normally results in fluorescence), can instead nonradiatively transition back to their ground state through a close encounter (collision or static binding) with a quencher (*37*). The relative potency of the quencher or, conversely, the relative accessibility of the fluorophore being quenched can be determined through Stern−Volmer analysis (eq 1):

$$\frac{\tau_0}{\tau_Q} = 1 + K_Q[Q] \quad (1)$$

where the fluorescence lifetimes of the fluorophore in the absence of quencher (τ_0) and in the presence (τ) of a certain concentration of quencher [Q] are used to calculate a quenching constant K_Q.

Assuming that the quenching is purely collisional or dynamic (i.e., that no stable, long-lived complexes form between the quencher and the fluorophore), the fluorescence lifetime can be linearly correlated to the fluorescence intensity measured in these experiments (F) ($t \propto F$), leading to eq 2:

$$\frac{F_0}{F_Q} = 1 + K_Q[Q] \quad (2)$$

During the titrations, we observed a time-dependent drift of the baseline that was close to linear on the time scale of the experiment. To correct for this, each quenching curve was recorded under identical conditions with the addition of quencher at precisely and evenly timed intervals and analyzed by eq 3:

$$F_Q = \frac{F_0}{1 + K_Q[Q]} - b[Q] \quad (3)$$

Equation 3 represents a rearranged Stern−Volmer equation, with a linear correction with slope b. In this equation, the b[Q] term represents the time-dependent variation in baseline fluorescence, where time is represented by the quencher concentration, which, in the experimental titration, increases by the same amount at evenly spaced time points. In the initial analysis, eq 3 was fit to each quenching data set obtained at a given pH. In these fits, the experimentally determined values of F_0 were used (whose values in volts were close to unity); K_Q and b were treated as local variables. A linear function was then fit to a plot of b versus F_0 (for all pH points) resulting from this analysis; the resulting trend line was used to calculate a value of b (−0.491) for an F_0 of 1. Each individual quenching curve was then refit with F_0 globally set to 1 and b globally set to −0.491, with a sole local variable of K_Q.

The resulting data points (K_Q vs pH) were arranged into bins spanning 0.2 pH unit (representing the estimated error of ±0.1 pH unit associated with changing solvent composition during the titrations); average K_Q and pH values for each bin are shown in Figure 2, with error bars reflecting the standard error for K_Q within each bin. A protonation equilibrium function, defined by eqs 4 and 5, was fit to the unbinned data (fit function displayed as a solid line). The protein was assumed to be fully tetrameric under every condition studied (*10*).

$$K_{Q,obs} = \frac{K_{q0}M_0 + K_{q2}M_2 + K_{q3}M_3 + K_{q4}M_4}{M_0 + M_2 + M_3 + M_4} \quad (4)$$

In eq 4, K_{q0}, K_{q2}, K_{q3}, and K_{q4} represent the quenching constant of the fully deprotonated, doubly protonated, triply protonated, and quadruply protonted species of the protein, respectively. M_0, M_2, M_3, and M_4 represent the relative population of each species, respectively. When the pK_a values governing the protonation events are considered, eq 4 is expanded into eq 5:

$$K_{Q,obs} = \frac{K_{q0} + \frac{K_{q2}[H^+]^2}{K_{a12}{}^2} + \frac{K_{q3}[H^+]^3}{K_{a12}{}^2K_{a23}} + \frac{K_{q4}[H^+]^4}{K_{a12}{}^2K_{a23}K_{a34}}}{1 + \frac{[H^+]^2}{K_{a12}{}^2} + \frac{[H^+]^3}{K_{a12}{}^2K_{a23}} + \frac{[H^+]^4}{K_{a12}{}^2K_{a23}K_{a34}}} \quad (5)$$

In this model, each protonation state of the tetramer has a preferred equilibrium ensemble of structures, reflected in a specific K_Q determined by the intrinsic lifetime of Trp41 and its accessibility to quencher. Therefore, the observed K_Q is deconvolved into population-weighted components consisting of K_{Q0}, K_{Q2}, K_{Q3}, and K_{Q4} [with previously determined experimental pK_a values used as constraints (*29*)]. In this previous work, the first two protonation events appeared to occur over a narrow concentration

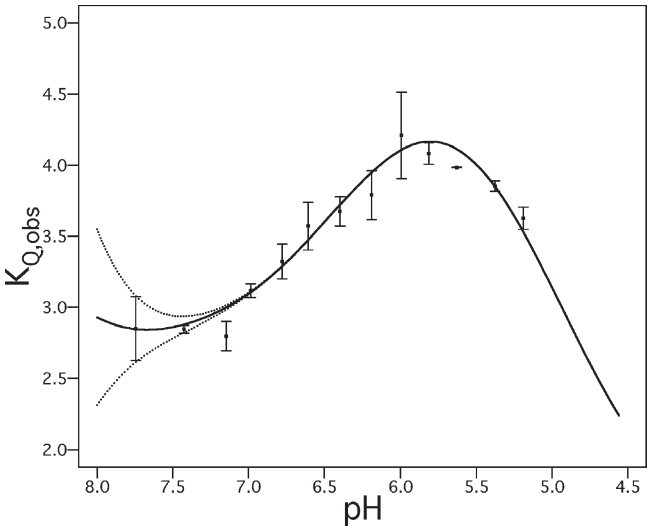

FIGURE 2: Experimentally calculated Stern−Volmer quenching constants of M2 Trp41 as a function of pH over a physiologically encountered pH range. To provide a more robust indication of experimental error, titration data points were binned in groups spanning 0.2 pH unit reflecting the experimental uncertainty of ~0.1 pH unit. Squares represent averages of pH and $K_{Q,obs}$ in each bin; error bars show the standard error associated with each bin (standard deviation of the $K_{Q,obs}$ values within each bin divided by the square root of the number of points in the bin). The data can be deconvoluted into an ensemble of distinct conformations with pH transition midpoints constrained as experimentally observed M2 pK_a values (*29*) (—). Because the fully neutral (+0) protonation state is almost completely absent at physiological pH, there is greater uncertainty with regard to the corresponding conformation's quencher accessibility (dotted lines represent uncertainty limits of the deconvolution fit for the neutral state). The deconvoluted K_Q values and fit uncertainities (in units of M^{-1}) for each protonation state are as follows: $K_{Q0} = 3.4 \pm 2.2$, $K_{Q2} = 2.7 \pm 0.1$, $K_{Q3} = 5.1 \pm 0.2$, and $K_{Q4} = 1.2 \pm 0.4$.

range with a midpoint of 8.2. We therefore treat them as a cooperative two-proton transition. The fourth pK_a was estimated to be less than 5.0 in the previous study. Similarly, we find the best fit to the experimental data (for a physically reasonable K_{Q4} of $\geq 1\ M^{-1}$) when this parameter is in the range of 4.9−5.0. In the fits shown in Figure 2, the fourth pK_a was fixed at 5.0; a very similar best-fit line and fit quality were obtained when it was set to 4.9.

Functional Reconstitution of M2 into Liposomes. The Cys-free, Trp15Phe His-tagged M2 construct used for fluorescence studies was expressed as previously described (*10*). After elution from the nickel column, the protein was desalted, concentrated, and exchanged into a final solution of 20 mM HEPES (pH 8), 4 mM OG, and 20% (v/v) glycerol using centrifugal concentrators (Millipore, Billerica, MA).

The same 4:1:2 POPC/POPG/cholesterol lipid mixture was used for functional reconstitution assays, with protein added to a 5×10^{-4} protein (tetramer):lipid molar ratio. Prior to freeze−thaw cycles to form the liposomes, the fluorescent pH indicator hydroxypyrenetrisulfonic acid (HPTS or pyranine) was added to a concentration of 1 mM. Liposomes were reconstituted in K^+ buffer, consisting of 10 mM K_2HPO_4, 50 mM K_2SO_4, and 5 mM MOPS (pH 7.4). Samples were subjected to an additional 10−15 freeze−thaw cycles to promote encapsulation of dye molecules. Following extrusion to a target liposome diameter of 100 nm, liposomes were dialyzed for 48 h against two 2 L volumes of K^+ buffer to remove unencapsulated dye molecules and excess OG.

Proton Flux Assay. The measurement was taken on an ISS PC1 spectrofluorometer (ISS Inc., Champaign, IL) with 10 mm excitation and 4 mm emission path lengths and 0.5 mm slit widths for both the excitation and emission monochromators. The internal liposome pH was determined by the ratio of HPTS fluorescence intensities at 460 and 417 nm (460/417) by comparison with an HPTS pH calibration curve; 417 nm is a pH-independent isosbestic point for HPTS. For all measurements, the emission wavelength was set at 515 nm. To assess M2 activity, 10 μL of liposomes reconstituted in K^+ buffer were diluted into 990 μL of Na^+ buffer [10 mM Na_2HPO_4, 50 mM Na_2SO_4, and 5 mM MOPS (pH 7.4)]. Electrochemical gradients across the liposome membranes were generated by addition of 5 μL of 5 μM valinomycin. Immediately after the addition of valinomycin, time traces were recorded an excitation wavelength of 460 nm for 200 s at 10 s intervals. Immediately after collection of a time trace at 460 nm, the isosbestic point of HPTS (excitation at 417 nm) was also collected for 200 s at 10 s intervals. To probe amantadine inhibition of A/M2 activity, 1 μL of 100 mM amantadine HCl (Sigma-Aldrich) was added to Na^+ buffer and incubated for 5 min with liposomes prior to the addition of valinomycin. Control liposomes (with no A/M2 added during the reconstitution process) were also included in the assay. Experiments were performed in duplicate under each condition.

Measurements of pH-Dependent Currents through M2-Expressing Xenopus Oocytes. Measurements of current through M2 expressed in the *Xenopus laevis* oocyte system at varying bathing buffer pH values were taken as previously described (*41*). Briefly, M2 currents were measured before and after application of 100 μM amantadine for each pH value. Between each experimental pH value, the oocyte was bathed in a solution at pH 8.5. The amantadine-sensitive net current was calculated by subtraction of residual current after amantadine inhibition from maximum currents at each pH value before amantadine inhibition. Experiments were performed in triplicate under each condition. The resulting amantadine-sensitive current−pH_{out} relationship was used as one of the data sets in mechanistic model fitting (vide infra).

Steady-State Kinetic Mechanisms of M2 Conduction. Transporter models were developed to describe flux at steady-state kinetic regimes (i.e., immediately following the imposition of a driving force for proton transport), with the concentrations of H^+ inside and outside the membrane clamped at their set values for the analysis. Each model was constructed as a kinetic cycle of interconverting conformational and protonation states, with the simplest arrangement shown in Figure S1 of the Supporting Information, where each transition is defined by its own rate constant. In Figure 3, the same scheme is shown but certain rate constant pairs found to be non-rate-determining were converted into equilibrium constants for ease of presentation; a similar approach was taken with the more complex mechanism shown in Figure 5. The derivation of a steady-state proton flux equation from the model schematics is described in detail in the Supporting Information. Briefly, a system of equations was constructed by setting the sum of the rates of formation and depletion of each possible state of the protein to zero to reflect steady-state kinetics. The system was solved symbolically for the normalized population of each state as a function of rate constants and proton concentrations, and a flux equation was derived by subtracting the differences of the proton release and binding rates on either side of the membrane.

The resulting flux equation was then globally fitted to M2 functional data from a variety of sources, including data collected by the authors on M2 expressed in *Xenopus* oocytes, and

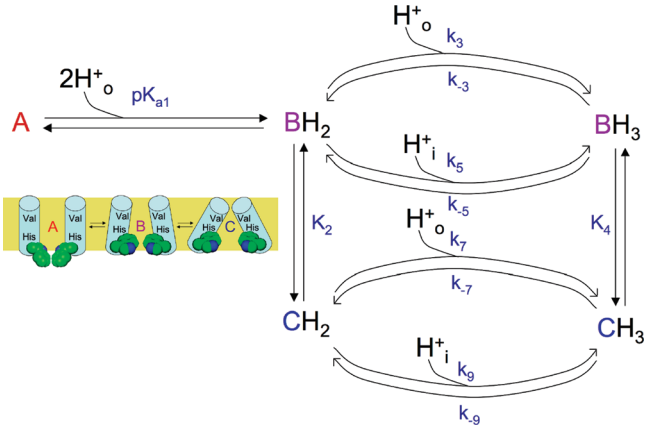

FIGURE 3: Two-state conduction mechanism presented as a kinetic scheme involving activation by low pH_{out}. H^+_o represents extraviral (N-terminal) protons, while H^+_i represents intraviral (C-terminal) protons. Proton binding and release occur on the horizontal axis, while conformational changes occur on the vertical axis in the scheme. The activating protons can be bound and released only externally. Minor "leak" pathways are described by k_5, k_{-5}, k_7, and k_{-7}.

experiments described by Chizhmakov et al. (*11*, *12*), where M2 was expressed in MEL cells. Global fitting was performed using the Levenberg−Marquardt algorithm implemented in Igor Pro 6.04 (*42*). Rate constants involving a charged species were modeled as voltage-dependent unless otherwise indicated, using an extension of the single-conformation electrical distance/barrier model developed by Lear (*36*) with additional conformational states and barriers added to describe the system (see Results and Discussion and Supporting Information). For kinetic cycles, one of the rate constants was not independently fit but instead calculated using microscopic reversibility from the remaining rate constants in the cycle at zero driving potential and equal pH_{in} and pH_{out} values.

RESULTS AND DISCUSSION

pH-Dependent Transitions of Full-Length M2 in Phospholipid Vesicles. To correlate structural transitions in M2 with the process of proton conduction, it was important to measure conformational changes under conditions where the protein demonstrates robust proton transport. The Cys-free, single-Trp construct used for fluorescence quenching studies was therefore reconstituted for flux measurements in a similar fashion, into phospholipid vesicles of the same composition and target size. The resulting proteoliposomes demonstrate amantadine-sensitive proton currents (Figure S2 of the Supporting Information) when flux is triggered by the addition of the ionophore valinomycin (*21*), unlike protein-free control vesicles that remain essentially proton-impermeable on the time scale of the experiment. This result confirms that M2 is active under the conditions used for spectroscopic studies of its conformation, allowing for correlation of conformational changes with transport phenomena.

Having demonstrated that this M2 variant was active in forming channels, we examined its fluorescence properties as a function of pH. Relatively small changes in M2 Trp fluorescence intensity and emission maximum have been reported previously; the studies of Hay and co-workers (*43*) were suggestive of a multistate process, but the degree of spectral perturbation was too small to allow more than a single transition to be observed. We therefore turned to collisional fluorescence quenching to report more fine-grained changes in the Trp41 environment. The great advantage of this method is that under a given condition, the protein is titrated with various concentrations of the quencher, allowing a multipoint determination of the quenching constant that is often more sensitive to environmental change and more precisely determined than the information derived from taking a single spectral scan. The Stern−Volmer quenching constant (K_Q) obtained from such experiments reflects the accessibility of a Trp residue along with other properties such as the intrinsic fluorescence lifetime, and environmental factors that can be more difficult to interpret. Here, however, very good structural data already exist for the protein, so we were primarily interested in using K_Q as a convenient intrinsic reporter of the Trp41 environment. We therefore examined the quenching of Trp41 by iodide and automated the titrations to maximize run-to-run reproducibility and to allow a constant correction for instability in the Trp41 signal (see Materials and Methods). It is important to stress that the pH dependence of the quenching constant is being measured here as a reporter of conformational change to allow definition of the number of spectroscopically distinct states, rather than in an attempt to provide detailed information about the specific conformational forms.

The relationship of the Stern−Volmer quenching constant for M2 Trp41 ($K_{Q,obs}$), calculated by fitting eq 4 to quenching titration data sets collected over a pH range of ~5−8, is plotted versus experimental H^+ concentration in Figure 2. A triphasic pH dependence of $K_{Q,obs}$ is observed, with low quencher accessibilities at pH 7−8 that rise to a peak at pH ~6 and decline again at lower pH values. These data show that M2 adopts several different protonation states in this physiological pH range and that in each state the Trp41 residue has a distinct environment.

The position of the peak and inflection points in Figure 2 are consistent with the pK_a values previously reported by Cross and co-workers for His37 in phospholipid bilayers (*29*). In particular, the low K_Q values at high pH would be associated with the neutral to +2 states (pK_a = 8.2), the peak near pH 6 is consistent with the formation of the +3 state (pK_a = 6.3), and the falloff at low pH is consistent with additional protonation to form the +4 state. Indeed, a theoretical curve calculated using the pK_a values determined by Hu et al. gives a very good fit to the data (Figure 2, solid line). Because the pK_a values were already known from the work of Cross and colleagues, the curve in Figure 2 was generated by fixing these pK_a values and using K_Q values for the individual protonation states as the only adjustable parameters. The values of K_Q increase from the +2 to +3 states and then decrease again as the +4 state becomes populated. It is difficult to place an unambiguous interpretation on the magnitudes of K_Q for each species, because the differences in K_Q are relatively small (2-fold) over the range studied. Moreover, exhaustive studies using different quenching agents were beyond the scope of this work. There also is a relatively large error associated with the quenching constants for the neutral and +4 states, because the pK_a values of the system are such that these two states are in low abundance over the physiological pH range studied here. Nevertheless, the data clearly show distinct accessibilities for the different protonation states. It is also interesting to correlate the decrease in quencher accessibility at low pH with the findings of Howard and co-workers, who observed that the C-terminal helix following the M2 transmembrane bundle became more deeply embedded in the bilayer near pH 5 (*44*). Linked transitions of the C-terminal helix may therefore play some role in the decreased Trp41 accessibility at low pH.

In summary, these findings allow us to correlate physiologically encountered protonation events of the M2 tetramer with conformational transitions of the transmembrane domain observed under conditions where the protein is functional. In particular, our data indicate that binding and release of the third and fourth protons by M2 lead to significant conformational changes in the protein. We next examine mechanistic models for conduction where protonation and deprotonation events drive conformational changes in M2 that affect the rates of permeant proton binding and release.

Conductance Models of Transport in Which Proton Uptake and Release Rates Are Mediated by H^+-Driven Changes in Structural Equilibria Yield Good Fits to Multiple Electrophysiological Data Sets. Previous electrophysiological experiments by Chizhmakov et al. and Pinto et al. have provided a wealth of pH-dependent current−voltage curves for the M2 proton channel expressed in mammalian cells and *X. laevis* oocytes (*11*, *12*, *18*, *20*). While progress has been made in describing the entire body of electrophysiological results, a single model that provides a complete description of all aspects of the conductance curves has been elusive (*11*, *15*, *26*, *35*, *36*). The current observation of multiple conformational and protonation states over the pH range used in electrophysiology experiments provides a rationale for developing a proton transport model that links His37 protonation events with structural transitions in the M2 transmembrane bundle, which in turn influence proton stability, accessibility to solvent from the N-terminal and C-terminal side of the pore, and maximal rate of proton release. A key conceptual foundation of this analysis is the distinction between conformational equilibria of the M2 tetramer bundle (Figure 1, where the protein populates some combination of states A, B, and C) and protonation equilibria at the His37 tetrad (states +0 to +4), which in the model influence the population of each distinct conformational state. Thus, His37 tetrad protonation states and M2 conformations are distinct but thermodynamically and functionally interrelated entities.

We initially examined the model shown in Figure 3, which is a refinement of the previously proposed two-state transporter mechanism (*34*). According to this hypothesis, the first two protons bound from the extraviral compartment activate the protein to enter the conduction cycle; the first two protons themselves are not permeant in this model and cannot be released to the C-terminal side of the membrane. Evidence for protonation-mediated M2 activation comes from experiments (*11*) in which it was shown that with an outward-driving transmembrane potential, the level of transport through M2 decreased at more basic pH_{out} values in spite of an increasing gradient for outward proton flux and from experiments in which the C-terminal pH was lowered to create a pH gradient but did not result in outward current flow (*18*). These observations suggested that the protein was populating an inactive state at high external pH. In the model shown in Figure 3, the low net outward conductance at high pH_{out} can be qualitatively explained by the kinetic trapping of the protein in the nonconducting A conformation (Figure 1), in which the His tetrad has low accessibility to protons from the C-terminal side. Of the known high-resolution structures, this conformation is presumably most similar to the high-pH solution NMR structure (*31*), which is partially open on the N-terminal side and nearly fully closed at the C-terminus.

At lower pH_{out} values, we postulated that the first two protons bound convert the A conformation, significantly populated only in the +0 His37 tetrad state, and described by the high-pH NMR structure (*31*), into an ensemble of B and C conformations. The structures suggest that the B and C conformers have successively more constricted N-terminal and dilated C-terminal pore regions, but this is not an implicit assumption of the conduction model. On the basis of structural studies, the B conformation is likely similar to an intermediate-pH crystal structure (*33*), a solid-state NMR structure (*45*, *46*), and computational models (*34*, *35*). These differ from the A conformation by virtue of a more open cytoplasmic end of the pore (Figure 1). Finally, the C conformation is likely to resemble the conformations seen in crystal structures, which have splayed C-terminal (inner facing) helices and a closed N-terminal end facing the outside of the virus (*32*). We therefore schematically show the C-terminal end of the channel to dilate in the figure, although it is important to emphasize that the kinetic conductance model does not presuppose anything other than that there are distinct conformational states with differing accessibilities and affinities for protons. The stabilities of these conformational states of the M2 bundle depend on pH, in such a way that increasing the level of protonation of the His37 tetrad favors formation of the C conformation, thereby allowing hydration and minimizing repulsions between His37 residues on adjacent monomers. However, each distinct protonation state has an equilibrium mixture of conformational states (and vice versa), so it is again important not to equate a given His37 tetrad protonation state with a unique conformational state.

A number of independent experimental restraints constrained the fitting process. The pK_a values for binding the first two protons (describing the transition from a fully deprotonated conformation A to the doubly protonated conformation B) were fixed at 8.2, as measured by Cross and colleagues (*29*). This double-protonation event was treated as a rapid equilibrium, relative to conduction at the pH where the A conformation is largely populated, because of the lack of activation of the channel and the low concentrations of permeant protons. Second, as supported by our fluorescence quenching results, we expected that binding of the third proton by the doubly protonated conformation B shifted the structural equilibrium toward conformation C; correspondingly, using the principles of microscopic reversibility and linked equilibria, the model was constrained such that the third proton pK_a of conformation C was greater than the third proton pK_a of conformation B. We did not explicitly constrain the actual fitted pK_a values for the third protonation step to be anything other than experimentally feasible (in the range of 2−10). However, we used the best-fit results of these values to calculate an averaged third proton pK_a weighted according to the relative population of the B and C conformations predicted by our model (see the Supporting Information) and compared it to the value experimentally determined in bilayers (*29*). In the initial fitting process, on rates for principal protonation pathways (k_3 and k_9) were allowed to vary within reasonable ranges expected for diffusion-limited processes given the diameter of the pore (10^6−10^9 M^{-1} s^{-1}) (*25*). Finally, microscopic reversibility provided another restraint on the system, allowing us to directly calculate one parameter from the values of others. For example, $k_3/k_{-3} = k_5/k_{-5}$ and $k_7/k_{-7} = k_9/k_{-9}$, and K_4 is known from the values of these constants plus K_2. For the sake of completeness, we included the kinetic pathways, mediated by k_5, k_{-5}, k_7, and k_{-7}, in the fitting, but they did not contribute significantly to the fit and were eliminated (data not shown). This finding is consistent with the structural model showing that the B state would be more accessible to

protons on the outside than the C state ($k_3 > k_7$) and that the C state is more accessible to protons from the inside ($k_9 > k_5$). Thus, these pathways were not described further for this model.

In summary, the following parameters were allowed to float in the fitting process, some with constraints as described above: the third proton pK_a for conformations B and C and the corresponding proton on rate constants (k_3 and k_9), and the magnitude of the two rate constants making up the conformational equilibrium constant K_4. One of the rate constants making up K_2 was initially constrained to result in a rapid equilibrium (the other was calculated by microscopic reversibility). As we will see, even with the very large body of electrophysiological data available, these parameters were not uniquely defined, and multiple minima were observed. However, all but two of these could be ruled out because they predicted pK_a values that were far from those measured independently or the predicted conductance level was too low. Additionally, to account for the voltage dependence in the target data sets, the rate constants describing the binding, translocation, or release of the third proton were modeled as voltage-dependent using an approach adapted from Lear (*36*). The relative electrical distances for two conformations and three transition states were constrained to be equal or increase sequentially as the proton made its way from outside to inside the membrane and to fall between 0 and 1 (*36*).

This model was globally fit to current−voltage relationships for Weybridge A/M2 under several physiologically encountered pH conditions (*12*) (points, Figure 4, inset), pH-dependent chord conductance for Weybridge A/M2 (*11*) (points, Figure S3 of the Supporting Information), and a current−pH relationship for Udorn A/M2 (points, Figure 4); the current−pH relationships of the M2 variants from the Udorn and Weybridge strains are very similar (*47*). Because the absolute rate of conduction (in flux per tetramer) was not known for most of these experiments, the individually normalized relative rates of conductance were used for each curve. Multiple minima were found that provided adequate fits to the data. Applying the constraints described above, we found one solution that gave an overall, population-averaged third proton pK_a (~6.9) near the experimental pK_a value (6.3) for the third protonation of the M2 bundle (*29*) (see the Supporting Information for the equation). The conformation-specific third proton pK_a value was 6.0 for the B state and 7.5 for the C state (the full list of parameters is given in Table S1 of the Supporting Information). The results calculated from this solution are shown as solid lines in Figure 4 and Figure S3 of the Supporting Information. Excellent agreement was observed with experimental current−voltage curves (Figure 4, inset), and a very good fit to pH- and voltage-dependent chord conductances was obtained (Figure S3 of the Supporting Information). A good fit to the pH−proton flux relationship was also seen (Figure 4, main panel), although the model slightly underestimated the flux in intermediate- to low-pH regimes. These deviations are most likely secondary to the use of global fitting to obtain a single set of parameters. In its global nature, the fit was not optimized to a single buffer condition or changes due to the background expression system, and on the whole, the agreement with multiple data sets collected in different cell types and protein strains is remarkable. Encouragingly, the predicted per-tetramer proton flux with the best-fit model parameters (listed in Table S1 of the Supporting Information) was ~0.5 proton/s at pH_{out} 7, ~30 protons/s at pH_{out} 5 (pH_{in} 7.25, $V = -20$ mV), and ~90 protons/s at pH_{out} 5, pH_{in} 7.25, and $V = -130$ mV, consistent with the range of experimentally determined values in the literature (*10*, *22*, *23*).

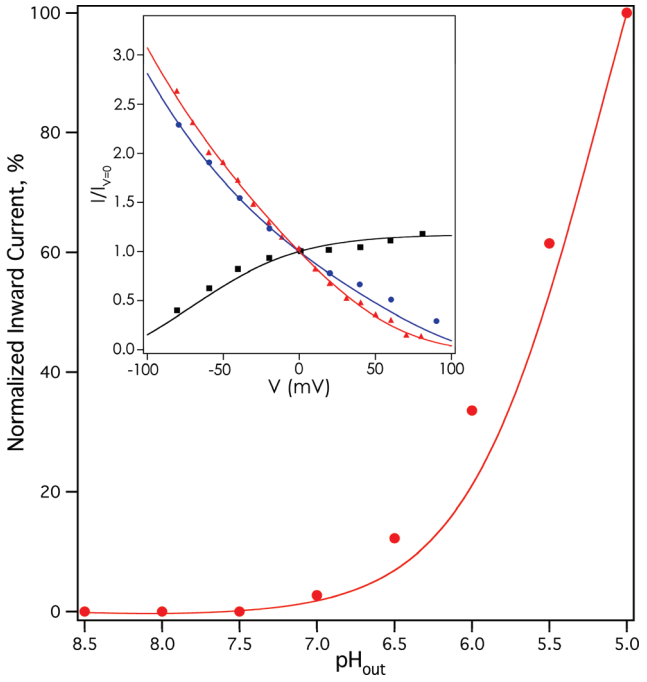

FIGURE 4: Results of fitting the activated two-state mechanism to M2 functional data. The inset shows rimantadine-sensitive current−voltage relationships of Weybridge A/M2 (data from ref *12*) at pH_{in} 7 and pH_{out} 5 (red triangles), pH_{in} 6 and pH_{out} 8 (black squares), and pH_{in} 8 and pH_{out} 6 (blue circles). The main panel shows the amantadine-sensitive current−pH_{out} relationship of Udorn A/M2 at −20 mV. Rimantadine-insensitive leak currents have been subtracted for each measurement in the inset; amantadine-insensitive leak currents have been subtracted for each measurement in the main panel.

We also observed a second good fit with reasonable specific activity and population-normalized pK_a when the relationship of the third proton pK_a values for the B and C conformations was reversed (i.e., forcing $pK_{aB} > pK_{aC}$). The ratio of the best-fit equilibrium constants K_2 and K_4 was also identically reversed, because of thermodynamic coupling. The fit quality in this case was essentially identical to the solution described above and is not presented graphically. The model parameters for this solution are shown in the right column of Table S1 of the Supporting Information. This result remains consistent with the structural model but suggests a reverse order of stability for the C versus B conformations with a decreasing pH. Under these conditions, because of the reversal of the ratio of K_2 and K_4, binding of the third proton now shifts the B−C conformational equilibrium to favor the B state. While this scenario is less consistent with the structural mechanism of progressive N-terminal pore closure and C-terminal pore dilation with a decreasing pH_{out}, it cannot be ruled out on the basis of electrophysiological data alone.

We also used this model to explore whether the conformational transitions (pathways described by K_2 and K_4 in Figure 3), or proton release from His37 (described by k_{-3} and k_{-9} in Figure 3), better corresponded to the rate-limiting process of conduction. Toward this end, when we applied our initial constraints, we treated the conformational transition between BH_2 and CH_2 (described by K_2) as a rapid, non-rate-determining equilibrium but allowed the rate constants making up K_4, which accounts for the interconversion of BH_3 and CH_3, to access both the rate-determining and non-rate-determining range. The initial

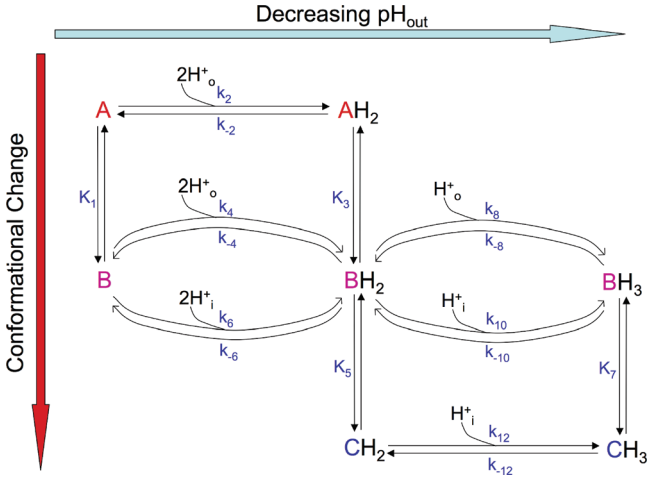

FIGURE 5: Augmented, multistate proton transport model, in which at least three conformations take part in the conduction cycle. Protonation and deprotonation events are shown on the horizontal axis, while conformational changes are shown on the vertical axis. The first two protons bound can now be conducted by the A and B conformations, while the third proton is conducted by the B and C conformations. H^+_o represents extraviral (N-terminal) protons, while H^+_i represents intraviral (C-terminal) protons. k_4, k_{-4}, k_{10}, and k_{-10} represent leak pathways.

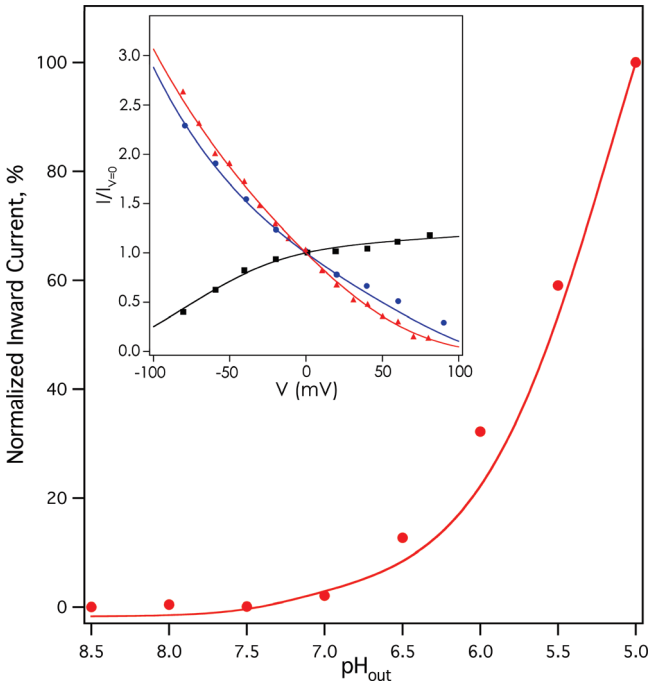

FIGURE 6: Results of fitting the augmented, multiconformation model to M2 functional data. Data are shown as in Figure 4.

model run converged on a solution where both conformational equilibria were rapid, and thus not rate-determining for transport ($k_{-4} \gtrsim 200\ s^{-1}$, and k_4:$k_{-4} \sim 10$:1), leading to the specific activity values described in the paragraph above. In the setting of the constrained, best-fit solution, we attempted to force the K_4 equilibrium to be rate-determining. This was done by gradually lowering the fixed value of k_{-4} from the starting value of 100 s^{-1} and keeping fixed the best-fit k_4:k_{-4} ratio of approximately 10:1 while simultaneously floating the rate constants for third proton binding (k_3 and k_9). The solutions under these conditions led to a similar fit quality for relative normalized rates but resulted in significant lowering of the predicted specific activity (e.g., ~30 protons per second per tetramer for $k_{-4} = 100$ and ~12 protons per second per tetramer for $k_{-4} = 50$, at pH_{out} 5, pH_{in} 7.25, and $V = -130$ mV). Repeating this simulation, while simultaneously forcing the K2 equilibrium to be slow, resulted in similarly low specific activities or negative best-fit on rate constants. Similar simulations that primarily constrained the equilibrium described by K_2 to be rate-determining and released the rate constants for third proton binding with or without simultaneously slowing the interconversion described by K_4 again resulted in negative on rate constants. We therefore find that under experimental constraints, the model is more consistent with literature specific activity values (*10*, *15*, *22*) when the rate of transport is limited by His37 deprotonation.

Some mutants of M2 exhibit biphasic conductance with pH, showing a main transition near pH 6, but also a small transition at higher pH values (*27*). Preliminary models suggested this might arise from a small degree of conduction of the first two protons bound by the tetramer through an equilibrium involving the A and B conformations, instead of having these protons play a purely activating role. We therefore wondered whether the neglect of conductance through these states by the model shown in Figure 3 might give rise to a positive deviation of the data from the theoretical curve near pH 6.5 in Figure 4. To address this issue, we examined an augmented transporter model (Figure 5), which differs from the simpler model (Figure 3) in that both A and B conformations are assumed to be populated in the His-neutral tetrad state. The principal pathways for conduction call for the A conformation to bind the first two protons and undergo a conformational change to the B conformation, which now can mediate their inward release by having some degree of accessibility to C-terminal pore waters. The doubly protonated B state can also bind a third proton supplied from the N-terminal side, with inward proton release following conformational change to the C state. Once again, minor leak pathways were initially incorporated in the calculations but did not significantly improve the goodness of fit. The augmented model was constrained essentially as for the simpler model described above, but the on rates and pK_a values for the first two protons bound were now allowed to float with constraints applied in a manner similar to the manner for those for the third protonation event in the simpler model. Given the results from the simpler model, conformational transitions were modeled as rapid equilibria. An additional set of electrical distances was fit for the translocation of the first two protons bound by the tetramer. The population-normalized pK_a values for binding of the first two protons and the third proton were again compared for consistency with solid-state NMR measurements (*29*) and were within 0.7 pK_a unit for the first two protons and within 0.6 pK_a unit for the third. The fitting results are shown in Figure 6 and Figure S4 of the Supporting Information, and a full list of fitting parameters is provided in Table S2 of the Supporting Information.

The fits to current−voltage data and flux−pH data were only very slightly improved as compared to the simpler model (Figure 6). The fit to chord conductance data was approximately the same (Figure S5 of the Supporting Information; with these parameters, the function exhibits a visible discontinuity at 60 mV because of software rounding error). The fitted pK_a values for binding of the third proton by the B and C states (6.0 and 7.5, respectively) were identical to those in the simpler model. Allowing transport of the first two protons bound by the A and B states led to fitted average pK_a values of 7.1 and 7.8, respectively (14.3 and

15.6 for the pK_a sums for the first two protons). On the whole, when compared to the fit results of the simpler model (Figure 4 and Figure S3 of the Supporting Information), the added complexity of the augmented multistate model (Figure 6 and Figure S4 of the Supporting Information) did not significantly improve the overall quality of the global fit. This finding suggests that for wild-type M2, transport of the first two protons bound contributes fairly little to overall conduction, although this state clearly contributes more to the pH−flux curves exhibited by certain M2 transmembrane domain mutants (*27*).

CONCLUSIONS

In this work, we have shown that M2 functionally reconstituted in bilayers undergoes pH-dependent transitions in its structural equilibrium that are described well by protonation and deprotonation events in the protein tetramer, allowing us to link conducting proton binding and release with structural changes. We find support for at least three conformations or conformational ensembles being involved in activation and/or conduction by wild-type M2 at physiologically encountered pH ranges.

The mechanistic flux models presented here lead to a simple physicochemical explanation for the highly complex electrophysiological behavior of this minimalistic membrane protein, which has been a topic of significant debate since the initial channel-like and shuttle-like mechanistic hypotheses were proposed (*14*, *28*). The fit results shown here suggest that both the saturation of the rate of proton flux through M2 at low pH and its preferred inward proton flux can be explained by protonation-driven shifts in the structural equilibrium that alternately expose the His37 side chain to external or internal solvent.

The results of fitting binding and rate constants emphasize the need to use multiple starting values to explore different possible solutions, as well as the need to acknowledge the limitations of this type of model. One major difference between this work and structure-based models (*26*) is that while structural models test whether a given set of experimental and MD structures can account quantitatively for the electrophysiological data, we instead search for all possible solutions that are consistent with a set of experimental observations, in this case the finding of three conformational states, and the known pK_a values for protonated His37. One of our expectations from the pH dependence of M2 conformations, seen here by fluorescence quenching and suggested in other structural and computational studies (*31*−*35*), was that the third protonation of the C conformational state would be more favorable than that of the B state, resulting in a greater stability of C than B in the +3 His37 tetrad state. Although this scenario was found to give a good fit to the data, a second, equally good solution was observed in which the B- and C-state pK_a values were reversed. Thus, while the study presented here is consistent with results of MD simulations and structural studies that suggest that multiprotonation of His37 results in overall dilation of the C-terminal end of the bundle, it is not possible to distinguish this model from the reverse scenario based on electrophysiological data alone. This finding underscores the need to consider different types of data (i.e., structural and functional) in developing a given model and indicates that the order of pK_a values for B versus C cannot be determined solely from the functional data sets used to fit the model.

M2 shows some of the characteristics of a transporter, in that its overall rate of conductance is relatively slow at physiological concentrations of its permeant ion (*25*), it undergoes conformational transitions in response to binding its conducted cargo (protons), and these conformational transitions occur on the same time scale as conductance (*31*). Moreover, our results suggest that dissociation of a proton from the channel rather than the modeled B-to-C conformational change limits the overall rate of conduction. This is consistent with deuterium isotope effects (*15*), but neither of these results rules out additional conformational transitions within the C state that are required for deprotonation to take place. In an environment as crowded as the end of the M2 channel, conformational transitions would almost certainly be linked to protonation and/or deprotonation at some level and hence are expected to be necessary for the exit of protons from the channel.

The M2 channel also shows many similarities to classical gated ion channels. For sake of simplicity, in the discussion given above, we suggest that the third proton binds to the His37 tetrad as it transits through the channel. This is clearly an oversimplification, as a new, high-resolution structure of the channel suggests that a conducting proton is statistically and possibly also quantum mechanically delocalized over a cluster of water and His residues (*33*). In this case, the conduction process through a large segment of the pore would occur over a relatively flat energy surface similar to that envisioned in continuum models for channels (*48*). Nevertheless, the mathematical modeling used in this site-binding approach would be functionally equivalent, but the interpretation of the rates would differ, as the saturation of rate would occur once a given level of occupancy of ions within this region of the channel is reached. Thus, as emphasized by Decoursey (*25*) and also exemplified in the steady progression of our structural understanding of potassium and cation channels (*49*, *50*), distinguishing site-binding from continuum models of conductance, or even "transporters" from channels, can be reduced to a matter of semantics (*51*).

Finally, these results are also important for efforts to design new M2 inhibitors, because they suggest that the drug may encounter several structural forms of the protein in vivo, thus presenting a spectrum of potential target structures for drug development. Interestingly, the chemical properties of amantadine appear to render it a multiform inhibitor, with evidence of amantadine binding to low-pH (*32*), intermediate-pH (*45*), and high-pH conformations (*52*). Newer compounds that do not feature this universality would require very tight binding to their target conformation to shift the structural equilibrium to the targetable, drug-bound state.

SUPPORTING INFORMATION AVAILABLE

Details of transport model derivation, population-averaged pK_a calculations, Figures S1−S4, and Tables S1 and S2. This material is available free of charge via the Internet at http://pubs.acs.org.

REFERENCES

1. Skehel, J., and Wiley, D. (2000) Receptor binding and membrane fusion in virus entry: The influenza hemagglutinin. *Annu. Rev. Biochem. 69*, 531–569.
2. Zhirnov, O. (1990) Solubilization of matrix protein M1/M from virions occurs at different pH for orthomyxo- and paramyxoviruses. *Virology 176*, 274–279.
3. Pinto, L., and Lamb, R. (2006) The M2 Proton Channels of Influenza A and B Viruses. *J. Biol. Chem. 281*, 8997–9000.
4. Grambas, S., and Hay, A. (1992) Maturation of influenza A virus hemagglutinin: Estimates of the pH encountered during transport and its regulation by the M2 protein. *Virology 190*, 11–18.

5. Davies, W., Grunert, R., Haff, R., McGahen, J., Neumayer, E., Paulshock, M., Watts, J., Wood, T., Hermann, E., and Hoffmann, C. (1964) Antiviral activity of 1-adamantanamine (amantadine). *Science 144*, 862–863.
6. Bright, R., Shay, D., Shu, B., Cox, N., and Klimov, A. (2006) Adamantane resistance among influenza A viruses isolated early during the 2005−2006 influenza season in the United States. *JAMA, J. Am. Med. Assoc. 295*, 891–894.
7. Wang, J., Cady, S., Balannik, V., Pinto, L., DeGrado, W., and Hong, M. (2009) Discovery of spiro-piperidine inhibitors and their modulation of the dynamics of the M2 proton channel from influenza A virus. *J. Am. Chem. Soc. 131*, 8066–8076.
8. Kolocouris, N., Zoidis, G., Foscolos, G., Fytas, G., Prathalingham, S., Kelly, J., Naesens, L., and De Clercq, E. (2007) Design and synthesis of bioactive adamantane spiro heterocycles. *Bioorg. Med. Chem. Lett. 17*, 4358–4362.
9. Chen, B., Leser, G., Jackson, D., and Lamb, R. (2008) The influenza virus M2 protein cytoplasmic tail interacts with the M1 protein and influences virus assembly at the site of virus budding. *J. Virol. 82*, 10059–10070.
10. Ma, C., Polishchuk, A., Ohigashi, Y., Stouffer, A., Schon, A., Magavern, E., Jing, X., Lear, J., Freire, E., Lamb, R., DeGrado, W., and Pinto, L. (2009) Identification of the functional core of the influenza A virus A/M2 proton-selective ion channel. *Proc. Natl. Acad. Sci. U.S.A. 106*, 12283–12288.
11. Chizhmakov, I., Geraghty, F., Ogden, D., Hayhurst, A., Antoniou, M., and Hay, A. (1996) Selective proton permeability and pH regulation of the influenza virus M2 channel expressed in mouse erythroleukaemia cells. *J. Physiol. 494*, 329–336.
12. Chizhmakov, I., Ogden, D., Geraghty, F., Hayhurst, A., Skinner, A., Betakova, T., and Hay, A. (2003) Differences in conductance of M2 proton channels of two influenza viruses at low and high pH. *J. Physiol. 546*, 427–438.
13. Holsinger, L., Nichani, D., Pinto, L., and Lamb, R. (1994) Influenza A Virus M2 Ion Channel Protein: A Structure-Function Analysis. *J. Virol. 68*, 1551–1563.
14. Pinto, L., Dieckmann, G., Gandhi, C., Papworth, C., Braman, J., Shaughnessy, M., Lear, J., Lamb, R., and DeGrado, W. (1997) A functionally defined model for the M2 proton channel of influenza A virus suggests a mechanism for its ion selectivity. *Proc. Natl. Acad. Sci. U.S.A. 94*, 11301–11306.
15. Mould, J., Li, H.-C., Dudlack, C., Lear, J., Pekosz, A., Lamb, R., and Pinto, L. (2000) Mechanism for Proton Conduction of the M2 Ion Channel of Influenza A Virus. *J. Biol. Chem. 275*, 8592–8599.
16. Pinto, L., Holsinger, L., and Lamb, R. (1992) Influenza Virus M2 Protein Has Ion Channel Activity. *Cell 69*, 517–528.
17. Shimbo, K., Brassard, D., Lamb, R., and Pinto, L. (1996) Ion selectivity and activation of the M2 ion channel of influenza virus. *Biophys. J. 70*, 1335–1346.
18. Tang, Y., Zaitseva, F., Lamb, R., and Pinto, L. (2002) The Gate of the Influenza Virus M2 Proton Channel Is Formed by a Single Tryptophan Residue. *J. Biol. Chem. 277*, 39880–39886.
19. Wang, C., Lamb, R., and Pinto, L. (1994) Direct measurement of the influenza A virus M2 protein ion channel activity in mammalian cells. *Virology 205*, 133–140.
20. Wang, C., Lamb, R., and Pinto, L. (1995) Activation of the M2 Ion Channel of Influenza Virus: A Role for the Transmembrane Domain Histidine Residue. *Biophys. J. 69*, 1363–1371.
21. Schroeder, C., Ford, C., Wharton, S., and Hay, A. (1994) Functional reconstitution in lipid vesicles of influenza virus M2 protein expressed by baculovirus: Evidence for proton transfer activity. *J. Gen. Virol. 75*, 3477–3484.
22. Lin, T., and Schroeder, C. (2001) Definitive assignment of proton selectivity and attoampere unitary current to the M2 ion channel protein of influenza A virus. *J. Virol. 75*, 3647–3656.
23. Moffat, J., Vijayvergiya, V., Gao, P., Cross, T., Woodbury, D., and Busath, D. (2008) Proton Transport through Influenza A Virus M2 Protein Reconstituted in Vesicles. *Biophys. J. 94*, 434–445.
24. Pielak, R., Schnell, J., and Chou, J. (2009) Mechanism of drug inhibition and drug resistance of influenza A M2 channel. *Proc. Natl. Acad. Sci. U.S.A. 106*, 7379–7384.
25. Decoursey, T. (2003) Voltage-gated proton channels and other proton transfer pathways. *Physiol. Rev. 83*, 475–579.
26. Zhou, H. X. (2010) Diffusion-Influenced Transport of Ions across a Transmembrane Channel with an Internal Binding Site. *J. Phys. Chem. Lett. 1*, 1973–1976.
27. Balannik, V., Carnevale, V., Fiorin, G., Levine, B., Lamb, R., Klein, M., DeGrado, W., and Pinto, L. (2010) Functional studies and modeling of pore-lining residue mutants of the influenza A virus M2 ion channel. *Biochemistry 49*, 696–708.
28. Sansom, M., Kerr, I., Smith, G., and Son, H. (1997) The Influenza A Virus M2 Channel: A Molecular Modeling and Simulation Study. *Virology 233*, 163–173.
29. Hu, J., Fu, R., Nishimura, K., Zhang, L., Zhou, H.-X., Busath, D., Vijayvergiya, V., and Cross, T. (2006) Histidines, heart of the hydrogen ion channel from influenza A virus: Toward an understanding of conductance and proton selectivity. *Proc. Natl. Acad. Sci. U.S.A. 103*, 6865–6870.
30. Li, C., Qin, H., Gao, P., and Cross, T. (2007) Solid-state NMR characterization of conformational plasticity within the transmembrane domain of the influenza A M2 proton channel. *Biochim. Biophys. Acta 1768*, 3162–3170.
31. Schnell, J., and Chou, J. (2008) Structure and mechanism of the M2 proton channel of influenza A virus. *Nature 451*, 591–595.
32. Stouffer, A., Acharya, R., Salom, D., Levine, A., Di Constanzo, L., Soto, C., Tereshko, V., Nanda, V., Stayrook, S., and DeGrado, W. (2008) Structural basis for the function and inhibition of an influenza virus proton channel. *Nature 451*, 596–599.
33. Acharya, A., Carnevale, V., Fiorin, G., Levine, B. G., Polishchuk, A., Balannick, V., Samish, I., Lamb, R. A., Pinto, L. H., DeGrado, W. F., and Klein, M. L. (2010) Structural mechanism of proton transport through the influenza A M2 protein. *Proc. Natl. Acad. Sci. U.S.A. 107*, 15075–15080.
34. Khurana, E., Dal Peraro, M., DeVane, R., Vemparala, S., DeGrado, W., and Klein, M. (2009) Molecular dynamics calculations suggest a conduction mechanism for the M2 proton channel from influenza A virus. *Proc. Natl. Acad. Sci. U.S.A. 106*, 1069–1074.
35. Yi, M., Cross, T., and Zhou, H. (2009) Conformational heterogeneity of the M2 proton channel and a structural model for channel activation. *Proc. Natl. Acad. Sci. U.S.A. 106*, 13311–13316.
36. Lear, J. (2003) Proton conduction through the M2 protein of the influenza A virus; a quantitative, mechanistic analysis of experimental data. *FEBS Lett. 552*, 17–22.
37. Lakowicz, J. (2006) Quenching of Fluorescence. In Principles of Fluorescence Spectroscopy, 3rd ed., pp 278−330, Springer, New York.
38. Ladokhin, A., Jayasinghe, S., and White, S. (2000) How to measure and analyze tryptophan fluorescence in membranes, and why bother? *Anal. Biochem. 285*, 235–245.
39. Dvorin, E., Mantulin, W., Rohde, M., Gotto, A., Jr., Pownall, H., and Sherrill, B. (1985) Conformational properties of human and rat apolipoprotein A-IV. *J. Lipid Res. 26*, 38–46.
40. Stoeva, S., Dolashka, P., Bankov, B., Voelter, W., Salvato, B., and Genov, N. (1995) Spectroscopic properties of *Callinectes sapidus* hemocyanin subunits. *Spectrochim. Acta A51*, 1965–1974.
41. Ohigashi, Y., Ma, C., Jing, X., Balannik, V., Pinto, L., and Lamb, R. (2009) An amantadine-sensitive chimeric BM2 ion channel of influenza B virus has implications for the mechanism of drug inhibition. *Proc. Natl. Acad. Sci. U.S.A. 106*, 18775–18779.
42. Igor Pro, version 6.04 (2008) WaveMetrics, Lake Oswego, OR.
43. Czabotar, P., Martin, S., and Hay, A. (2004) Studies of structural changes in the M2 proton channel of influenza A virus by tryptophan fluorescence. *Virus Res. 99*, 57–61.
44. Nguyen, P., Soto, C., Polishchuk, A., Caputo, G., Tatko, C., Ma, C., Ohigashi, Y., Pinto, L., DeGrado, W., and Howard, K. (2008) pH-induced conformational change of the influenza M2 protein C-terminal domain. *Biochemistry 47*, 9934–9936.
45. Cady, S., Schmidt-Rohr, K., Wang, J., Soto, C., DeGrado, W., and Hong, M. (2010) Structure of the amantadine binding site of influenza M2 proton channels in lipid bilayers. *Nature 463*, 689–693.
46. Nishimura, K., Kim, S., Zhang, L., and Cross, T. A. (2002) The closed state of a H^+ Channel Helical Bundle Combining Precise Orientational and Distance Restraints from Solid State NMR. *Biochemistry 41*, 13170–13177.
47. Wang, C., Takeuchi, K., Pinto, L., and Lamb, R. (1993) The ion channel activity of the influenza A virus M2 protein: Chacterization of the amantadine block. *J. Virol. 67*, 5585–5594.
48. Levitt, D. (1986) Interpretation of biological ion channel flux data: Reaction-rate versus continuum theory. *Annu. Rev. Biophys. Biophys. Chem. 15*, 29–57.
49. Gouaux, E., and MacKinnon, R. (2005) Principles of selective ion transport in channels and pumps. *Science 310*, 1461–1465.
50. MacKinnon, R. (2003) Potassium channels. *FEBS Lett. 555*, 62–65.
51. Miller, C. (2006) ClC chloride channels viewed through a transporter lens. *Nature 440*, 484–489.
52. Hu, J., Asbury, T., Achuthan, S., Li, C., Bertram, R., Quine, J., Fu, R., and Cross, T. (2007) Backbone structure of the amantadine-blocked trans-membrane domain M2 proton channel from influenza A virus. *Biophys. J. 92*, 4335–4343.